

Competition between phonon-vacancy and four-phonon scattering in cubic boron arsenide by machine learning interatomic potential

Jialin Tang,^{1,2} Guotai Li,^{2,3} Qi Wang,² Jiongzhi Zheng,⁴ Lin Cheng,² and Ruiqiang Guo^{2,*}

¹*Institute of Advanced Technology, Shandong University, Jinan, Shandong 250061, China*

²*Thermal Science Research Center, Shandong Institute of Advanced Technology, Jinan, Shandong 250103, China*

³*Institute of Thermal Science and Technology, Shandong University, Jinan, Shandong 250061, China*

⁴*Thayer School of Engineering, Dartmouth College, Hanover, New Hampshire 03755, USA*



(Received 28 December 2022; revised 20 March 2023; accepted 24 March 2023; published 10 April 2023)

Point defects can strongly suppress the thermal conductivity κ of solid materials, which is crucial for a broad range of applications, such as thermal management of electronic devices and thermoelectrics. Understanding thermal transport in materials containing point defects often relies on atomistic simulations based on density functional theory (DFT) or empirical potentials (EPs). However, modeling thermal transport in defective materials using DFT is very computationally expensive or even prohibitive due to the breaking of crystal symmetry while EPs suffer from low accuracy. Recently, machine learning has been applied to the development of interatomic potentials, offering opportunities to model defective systems accurately and efficiently. Here, we present a Gaussian approximation potential (GAP) developed for crystalline cubic boron arsenide (c-BAs) with vacancies, which can achieve DFT-level accuracy in predicting its κ and phonon transport properties at four orders of magnitude reduced computational cost, especially for phonon-vacancy and four-phonon scatterings. Particularly, we applied the GAP to investigate the effect of vacancies on the κ of c-BAs by considering both three-phonon and four-phonon scattering. Special attention was paid to the competition between phonon-vacancy and four-phonon scattering, which tend to decrease and increase the temperature dependence of κ , respectively. Specifically, when the vacancy concentration is much lower than 0.07% ($2.56 \times 10^{19} \text{ cm}^{-3}$), four-phonon scattering plays stronger roles in determining the temperature dependence of κ . As the vacancy concentration increases to 0.07%, the temperature dependence of κ becomes close to that considering only three-phonon scattering, indicating the comparable effect of phonon-vacancy and four-phonon scattering. As the vacancy concentration further increases, the phonon-vacancy scattering becomes more dominant and pushes the κ towards a temperature-independent behavior. Our work deepens the understanding of the phonon scattering landscape in c-BAs with vacancies and will be helpful for tailoring its thermal properties. Atomistic simulations combined with machine learning interatomic potentials are expected to be able to greatly advance the understanding of thermal transport in defective materials.

DOI: [10.1103/PhysRevMaterials.7.044601](https://doi.org/10.1103/PhysRevMaterials.7.044601)

I. INTRODUCTION

Point defects widely exist in solid materials and can strongly affect material properties [1–3]. Particularly, doping is commonly used to modulate the electronic and optoelectronic properties of semiconductors [4–7]. However, the point defects introduced by doping can largely suppress the thermal conductivity κ of semiconductors, deteriorating heat dissipation and thus the performance of devices. For instance, the κ of cubic boron arsenide (c-BAs) is as high as 910–1390 $\text{Wm}^{-1} \text{K}^{-1}$ at room temperature in high-quality samples [8–10], while the existence of point defects decreases its κ to only 200 $\text{Wm}^{-1} \text{K}^{-1}$ [11]. On the contrary, the reduction of κ by dopants is beneficial for enhancing the heat-to-electricity conversion efficiency of thermoelectric materials. For example, the κ ($1.4 \text{ Wm}^{-1} \text{K}^{-1}$) of (Mg, Bi) codoped polycrystalline GeTe at 700 K is reduced by 53% compared

with its pristine value ($3.0 \text{ Wm}^{-1} \text{K}^{-1}$), resulting in 110% improvement in its dimensionless figure of merit [12].

Phonons, i.e., quantized normal modes of lattice vibration, are the major heat carriers in semiconductors and insulators [13]. Tailoring the thermal conductivity of crystals with point defects essentially requires a fundamental understanding of phonon-defect interaction, which often relies on atomistic simulations that can provide detailed information on energy transport and structural evolution at atomic level [14]. However, modeling crystals containing defects remains challenging for traditional atomistic methods based on density functional theory (DFT) [15,16] or empirical potentials (EPs) [17–20]. On one hand, although state-of-the-art DFT calculations can accurately describe interatomic interactions [21–23], they are computationally expensive or even prohibitive for materials with defects due to a large number of atoms and the breaking of crystal symmetry. Particularly, accurate interatomic force constants (IFCs) (including harmonic IFCs of pristine and defective structures, as well as anharmonic IFCs of pristine structures) are required for calculating the

*ruiqiang.guo@iat.cn

lattice thermal conductivity of materials containing point defects using the Green's function approach combined with the Peierls-Boltzmann transport equation (PBTE) [24–26]. However, calculating the harmonic IFCs of defective structures by DFT is often very expensive. Moreover, for materials with strong phonon scattering beyond the third order (such as c-BAs [27], aluminum antimonide (AlSb) [28], and indium phosphide (InP) [29]), one also needs to calculate the fourth-order and even higher-order IFCs of a large number of pristine supercells, which further increases the computational cost. On the other hand, EPs-based simulations are often computationally acceptable and have been widely used to model complex systems with defects [30–33]. However, EPs fitted by simple functional forms are usually less accurate and less transferable than *ab initio* calculations, which makes it difficult for EPs to precisely describe the subtle high-dimensional features of potential energy surfaces (PESs) of defective materials [34,35].

Recently, machine learning has emerged as a powerful approach for developing interatomic potentials [36–41], offering opportunities to model phonon transport in defective systems accurately and efficiently. Extensive efforts have been devoted to the development of machine learning interatomic potentials (MLIPs), including the Gaussian approximation potential (GAP) [36], the moment tensor potential (MTP) [37], the spectral neighbor analysis potential (SNAP) [38], the neural network potential (NNP) [39], the neuroevolution potential (NEP) [40], deep potential (DP) [41], etc. To date, MLIPs have been applied to understanding phonon transport and predicting thermal conductivity in various material systems, such as crystalline silicon with vacancies [35], bulk hexagonal boron nitride [42], graphene/borophene heterostructures [43], β -Ga₂O₃ [44], and amorphous silicon [45]. These MLIPs are demonstrated to be as accurate as DFT, with orders of magnitude reduced computational cost [35,43–46]. Despite the great success of MLIPs, MLIPs that can accurately describe both phonon-defect and phonon-phonon interactions beyond the third-order anharmonicity have been rarely reported.

In this work we develop an accurate GAP-type MLIP for crystalline c-BAs with vacancies, a typical example with high thermal conductivity that is sensitive to both phonon-defect and four-phonon scattering [11,27–29,47]. We show that our GAP can predict the thermal conductivity and phonon properties of c-BAs containing B or As vacancies with DFT-level accuracy at four orders of magnitude reduced computational cost. Specifically, the three-phonon, four-phonon, and phonon-vacancy scattering rates calculated by the GAP all agree well with the DFT benchmarks, demonstrating the accurate descriptions of the harmonic IFCs of pristine and defective crystals, as well as the anharmonic IFCs up to the fourth order of pristine crystals. Using the trained GAP, we study the effect of vacancies on the κ of c-BAs by considering both three-phonon and four-phonon scattering. Particularly, we look into the competition between phonon-vacancy and four-phonon scattering, which can decrease and increase the temperature dependence of the κ of c-BAs, respectively. Specifically, when the vacancy concentration reaches 0.07% ($2.56 \times 10^{19} \text{ cm}^{-3}$), the phonon-vacancy and four-phonon scattering play comparable roles in determining the temperature dependence of κ . As the vacancy concentration further increases, phonon-vacancy scattering becomes more

dominant in suppressing κ , leading to a much weaker temperature dependence of κ . Our work offers a deep insight into the phonon-scattering landscape in c-BAs with vacancies and demonstrates that MLIPs can serve as a powerful tool to understand and predict thermal transport properties of defective materials.

II. METHODOLOGY

A. Gaussian approximation potential

The Gaussian approximation potential method adopts the Gaussian process regression to carry out the PES fit. In this work, the atomistic structures are described by a set of two-body (2B), three-body (3B), and many-body (MB) descriptors. The total energy of the GAP is the sum of the 2B, 3B, and MB interactions [48]:

$$E = \delta^{(2B)} \sum_{ij} \varepsilon^{(2B)}(\mathbf{q}_{ij}^{(2B)}) + \delta^{(3B)} \sum_{ijk} \varepsilon^{(3B)}(\mathbf{q}_{ijk}^{(3B)}) + \delta^{(MB)} \sum_i \varepsilon^{(MB)}(\mathbf{q}_i^{(MB)}), \quad (1)$$

wherein the indices i , j , and k run over all atoms in the system, and δ represents the weighting factor. The 2B descriptor is the distance between two atoms in an atomic pair:

$$\mathbf{q}_{ij}^{(2B)} = |\mathbf{r}_i - \mathbf{r}_j|, \quad (2)$$

where \mathbf{r}_i and \mathbf{r}_j represent the position vectors of the i and j atoms, respectively. The 3B descriptor involves both interatomic distances and the angular relationship, with the expression given by

$$\mathbf{q}_{ijk}^{(3B)} = \begin{pmatrix} r_{ij} + r_{ik} \\ (r_{ij} - r_{ik})^2 \\ r_{jk} \end{pmatrix}. \quad (3)$$

The many-body interactions are described by the smooth overlap of atomic positions (SOAP) descriptor. The atomic environment of SOAP is represented by a local atomic neighbor density $\rho_i(\mathbf{r})$ resulting from the summation of the Gaussian function placed on each neighbor atom within a cutoff radius r_{cut} . The density $\rho_i(\mathbf{r})$ can be expanded in a basis set of the radial function $g_{(n)}(r)$ and the spherical harmonic function $Y_{lm}(\mathbf{r})$:

$$\rho_i(\mathbf{r}) = \sum_{nlm} c_{nlm}^{(i)} g_{(n)}(r) Y_{lm}(\mathbf{r}), \quad (4)$$

where $c_{nlm}^{(i)}$ is the expansion coefficient for atom i . The SOAP descriptor is given by the power spectrum elements of these expansion coefficients:

$$\mathbf{q}_i^{(MB)} = P_{m'l}^{(i)} = \frac{1}{\sqrt{2l+1}} \sum_m c_{nlm}^{(i)} (c_{n'l'm}^{(i)})^*. \quad (5)$$

The local atomic energy contribution $\varepsilon^{(d)}(\mathbf{q}_i^{(d)})$ is given by a linear combination of kernel functions $K^{(d)}$ and its weight coefficient $\alpha_i^{(d)}$:

$$\varepsilon^{(d)}(\mathbf{q}_i^{(d)}) = \sum_{t=1}^{N_t^{(d)}} \alpha_t^{(d)} K^{(d)}(\mathbf{q}_i^{(d)}, \mathbf{q}_t^{(d)}), \quad (6)$$

TABLE I. Hyperparameters for training GAP.

Hyperparameters	2B	3B	SOAP
r_{cut} (Å)	5.5	5.5	5.5
δ (eV)	10.0	3.7	0.07
Sparse method	Uniform	Uniform	CUR
Sparse points	50	200	650
Δr (Å)			1
n_{max}			12
l_{max}			12
σ_v^{energy} (eV/atom)	0.0005		
σ_v^{force} (eV/Å)	0.001		

where d is the corresponding descriptor, and the kernel function $K^{(d)}(\mathbf{q}_i^{(d)}, \mathbf{q}_i^{(d)})$ is a measure of the similarity between the previously observed atomic environment $\mathbf{q}_i^{(d)}$ and the to-be-predicted atomic environment $\mathbf{q}_i^{(d)}$. The main hyperparameters used for training GAP in this work are summarized in Table I. More details about the GAP methodology can be found in Refs. [49,50].

B. Generation of the training and testing databases

The training and testing databases contain both configurations of perfect c-BAs and those with vacancies. Specifically, the training database includes 180 configurations of perfect c-BAs, 55 configurations with a single B vacancy, and 55 configurations with a single As vacancy. We constructed our training database using the total energy and atomic forces of each configuration obtained from *ab initio* calculations. All DFT calculations were performed using the projector augmented wave (PAW) method [51] implemented in the Vienna *Ab initio* Simulation Package (VASP) [52], with the Perdew-Burke-Ernzerhof (PBE) form of generalized gradient approximation (GGA) [53] for the exchange-correlation functional and a cutoff energy of 400 eV. Firstly, the atomic configurations for training datasets were selected by selecting one snapshot every 80 time steps from *ab initio* molecular dynamics (AIMD) simulations, which were performed in the canonical ensemble (*NVT*: constant number of atoms, constant volume, and constant temperature) at 300 K with a $1 \times 1 \times 1$ k -point grid for Brillouin zone sampling. The time step was set to 0.5 fs. Then, self-consistent field (SCF) calculations were performed to record the total energies and atomic forces of the selected configurations with a $2 \times 2 \times 2$ k mesh. Using the same approach, we generated a testing dataset containing 42 configurations of perfect c-BAs, 35 configurations with a single B vacancy, and 35 configurations with a single As vacancy.

C. Thermal transport calculations

The lattice thermal conductivity is calculated by iteratively solving linearized PBTE:

$$\kappa_{\alpha\beta} = \frac{1}{k_B T^2 N \Omega} \sum_{\lambda} f_0(f_0 + 1) (\hbar \omega_{\lambda})^2 v_{\lambda}^{\alpha} F_{\lambda}^{\beta}, \quad (7)$$

where α and β are Cartesian components, T is temperature, k_B is the Boltzmann constant, N is the total number of q points, Ω is the volume of the unit cell, \hbar is the reduced Plank constant,

and f_0 is the phonon distribution function. ω_{λ} and v_{λ}^{α} are the frequency and the group velocity along α direction of phonon mode λ , respectively. In this work, F_{λ}^{β} is given by

$$F_{\lambda}^{\beta} = \tau_{\lambda}^0 (v_{\lambda}^{\beta} + \Delta_{\lambda}^{\beta}), \quad (8)$$

where τ_{λ}^0 is the phonon lifetime, which is based on the relaxation time approximation (RTA), and Δ_{λ}^{β} is a correction term obtained by the iterative scheme of PBTE that merges the inelastic phonon-phonon scattering processes. In this work the PBTE is solved using an iterative method for three-phonon scatterings rates ($\tau_{3\text{ph}}^{-1}$) only, while four-phonon ($\tau_{4\text{ph}}^{-1}$), phonon-isotope (τ_{iso}^{-1}), and phonon-vacancy ($\tau_{\text{ph-v}}^{-1}$) scattering rates are treated under RTA.

The τ_{iso}^{-1} is calculated as [54]

$$\tau_{\text{iso}}^{-1} = \frac{1}{N} \sum_{\lambda'} \left[\frac{\pi \omega^2}{2} \sum_{i \in \text{u.c.}} g(i) |\mathbf{e}_{\lambda}^*(i) \cdot \mathbf{e}_{\lambda'}(i)|^2 \delta(\omega_{\lambda} - \omega_{\lambda'}) \right], \quad (9)$$

where $g(i) = \sum_s f_s(i) [1 - M_s(i)/\bar{M}(i)]^2$ is the Pearson deviation coefficient of the masses $M_s(i)$ of isotopes s of atom i (found with relative frequency $0 < f_s(i) \leq 1$), and $\bar{M}(i) = \sum_s f_s(i) M_s(i)$ represents the average mass.

We adopted an exact Green's function approach to calculate $\tau_{\text{ph-v}}^{-1}$ [22–25]:

$$\tau_{\text{ph-v}}^{-1} = -\frac{f \Omega}{\omega V_d} \text{Im} \{ \langle \lambda | \mathbf{T}^+ (\omega^2) | \lambda \rangle \}. \quad (10)$$

Here, the \mathbf{T}^+ matrix is expressed as $\mathbf{T}^+ = (\mathbf{I} - \mathbf{V} \mathbf{G}_0^+)^{-1} \mathbf{V}$. For a vacancy, \mathbf{V} is simply the perturbation matrix of IFCs, which is defined as $\mathbf{V}_{i\alpha, j\beta}^K = (K'_{i\alpha, j\beta} - K_{i\alpha, j\beta}) / (M_i M_j)^{1/2}$ ($K'_{i\alpha, j\beta}$ and $K_{i\alpha, j\beta}$ are the harmonic IFCs of the defective and perfect structures, M_i and M_j are the pristine atomic masses at lattice sites i and j , respectively). The volume fraction of point defects f is defined as the ratio of the volume of defect atoms to total volume of the supercell, and V_d is defined as the volume of a point defect. ω and \mathbf{G}_0^+ is the frequency of the incident phonon and the retarded Green's function of the unperturbed crystal, respectively.

Calculating the lattice thermal conductivity κ requires harmonic and anharmonic IFCs. Here, we calculated the IFCs using both the GAP and DFT. For the DFT calculations implemented in VASP, we first relaxed the primitive c-BAs unit cell using a $12 \times 12 \times 12$ k mesh, with the energy and force convergence criteria set to 10^{-8} eV and 10^{-6} eV/Å, respectively. The cutoff energy was set to 400 eV. Based on the relaxed pristine c-BAs, we calculated the harmonic and anharmonic IFCs for a $4 \times 4 \times 4$ supercell (128 atoms) using the finite-displacement approach [55]. Specifically, the interaction distance was restricted to the fifth- and second-nearest neighbors for calculating the third- and fourth-order IFCs of pristine c-BAs, respectively. The defective supercell containing 127 atoms was constructed by removing an atom in a $4 \times 4 \times 4$ supercell. We relaxed the defective supercell using the same settings and then calculated the harmonic IFCs for the relaxed defective supercell using the finite-displacement approach. All the DFT calculations of IFCs were performed using the PBE with a $3 \times 3 \times 3$ k mesh.

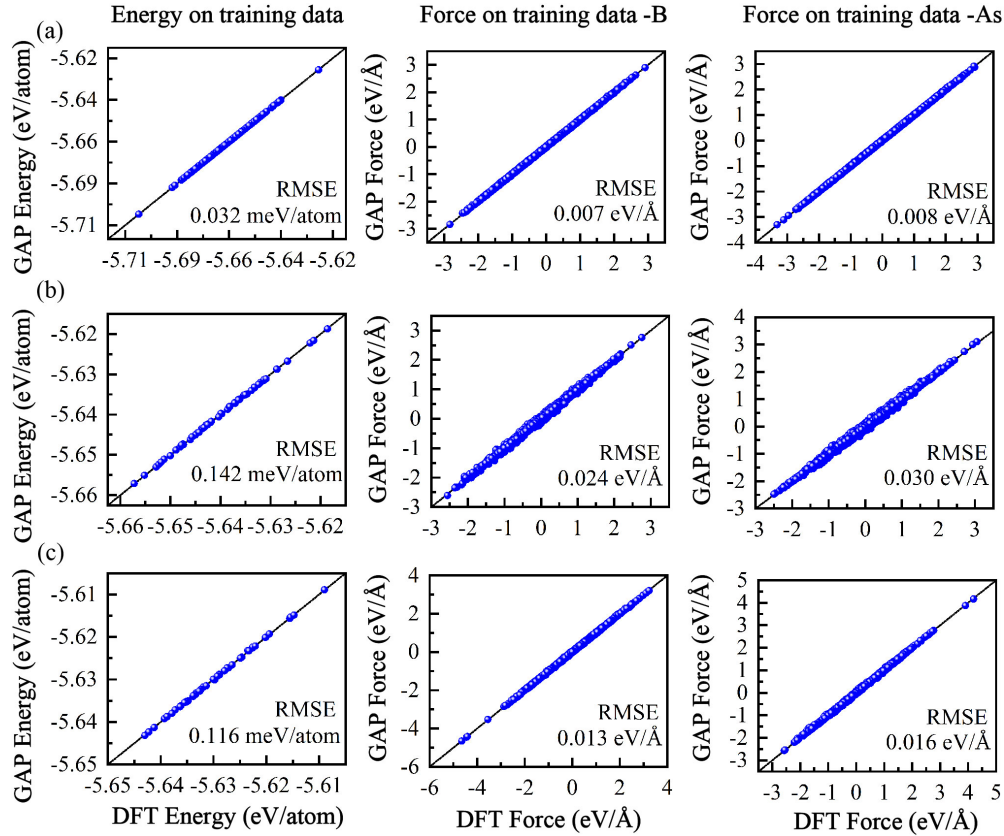


FIG. 1. Comparisons of atomic energies, atomic forces on B and As atoms calculated by the GAP and DFT for the (a) perfect, (b) B-vacancy-containing, and (c) As-vacancy-containing c-BAs in the training database.

Similarly, using the GAP implemented in the LAMMPS code [56], we relaxed the pristine and defective structures, and calculated all the harmonic and anharmonic IFCs. After obtaining the IFCs, the lattice thermal conductivity of c-BAs was calculated by iteratively solving linearized PBTE with a $16 \times 16 \times 16$ q mesh using the SHENGBTE [57] and the FOURPHONON module [58]. We show the convergence of the lattice thermal conductivity of c-BAs predicted by DFT with respect to the q mesh in Fig. S1 in the Supplemental Material [59].

III. RESULTS AND DISCUSSION

A. Evaluation of the GAP

We first validated the accuracy of the GAP model. As shown in Fig. 1, for both perfect c-BAs and that with vacancies in the training database, the atomic energies and forces predicted by the GAP are all in good agreement with the DFT benchmarks. Also, we calculated the root-mean-square errors (RMSEs) of atomic energies and forces between the GAP predictions and DFT benchmarks. For perfect c-BAs in the training database, the RMSE of atomic energies is 0.032 meV/atom, and the RMSEs of atomic forces are 0.007 eV/Å for the B atom and 0.008 eV/Å for the As atom [Fig. 1(a)]. For c-BAs containing vacancies in the training database, the RMSEs of atomic energies and forces increase to 0.142 meV/atom, 0.024 eV/Å, and 0.030 eV/Å for c-BAs with B vacancy, and 0.116 meV/atom, 0.013 eV/Å, and 0.016 eV/Å for that with As vacancy, as shown in Figs. 1(b)

and 1(c). This is expected considering that the inclusion of vacancies makes the PES more complex and increases challenges in fitting the PES. The small RMSE values demonstrate the high accuracy of the GAP for the in-domain data.

In Fig. 2, we show the atomic energies and forces predicted by the GAP and DFT for the testing databases. The RMSEs are 0.026 meV/atom, 0.006 eV/Å, and 0.008 eV/Å for perfect c-BAs in the testing database. These RMSEs are comparable to those of the training databases and smaller than those of previous GAP models for other crystalline materials, such as Si (0.027 eV/Å) [45] and Li (0.01 eV/Å) [60], indicating that the GAP has high accuracy in predicting the out-domain data. In comparison, the RMSEs of c-BAs containing vacancies in the testing database are relatively larger, which is expected considering vacancies complicate the PES. Specifically, the RMSEs increase to 0.130 meV/atom, 0.024 eV/Å, and 0.030 eV/Å for c-BAs with B vacancy, and 0.134 meV/atom, 0.017 eV/Å, and 0.017 eV/Å for that with As vacancy. We notice that these RMSEs of atomic forces are comparable to or smaller than those of reported GAP models for other crystals with vacancies (0.023 eV/Å) [61] and quinary MoNbTaVW alloy with vacancies (0.09 eV/Å) [62].

We continue to evaluate the performance of the GAP by comparing the lattice constants of the primitive unit cell. The lattice constant ($a = 4.79$ Å) predicted by the GAP is in good agreement with the DFT result ($a = 4.82$ Å). Also, the results predicted by both the GAP and DFT agree well with previous

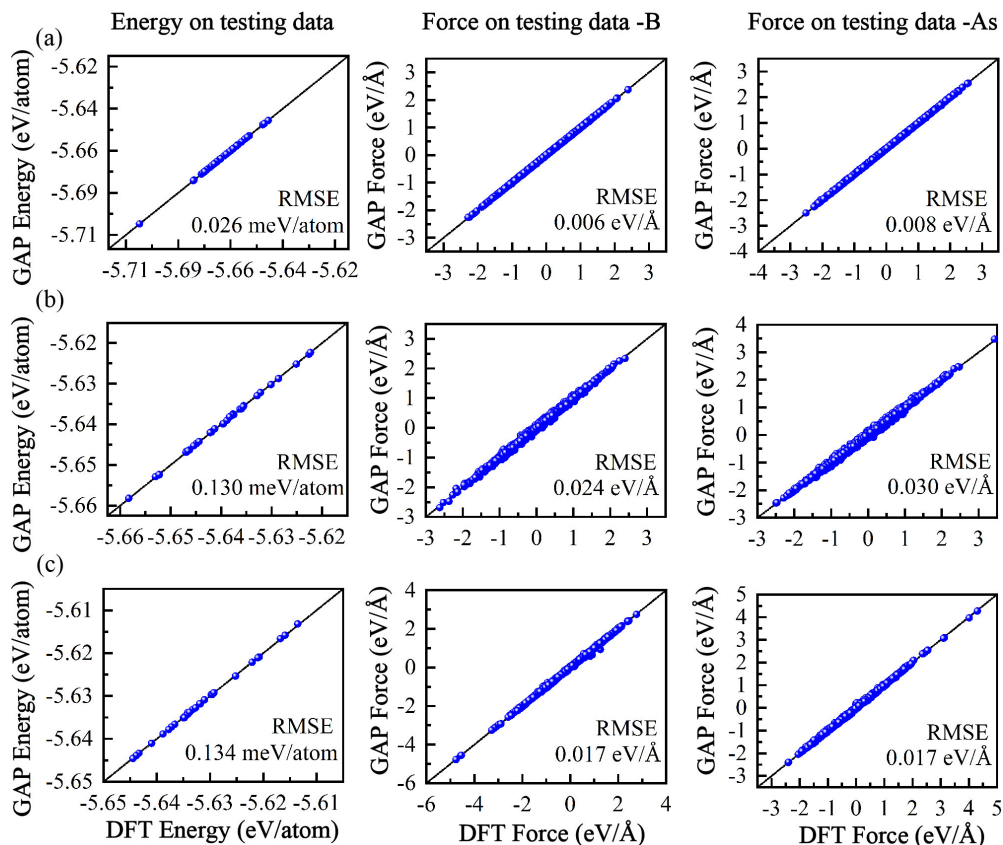


FIG. 2. Comparisons of atomic energies, atomic forces on B and As atoms calculated by the GAP and DFT for the (a) perfect, (b) B-vacancy-containing, and (c) As-vacancy-containing c-BAs in the testing database.

DFT ($a = 4.82 \text{ \AA}$) and experimental ($a = 4.78 \text{ \AA}$) results [11,47]. All these results demonstrate the high accuracy of the GAP in reproducing the *ab initio* PESs of perfect c-BAs and c-BAs with vacancies.

B. Accuracy of the GAP in Predicting Phonon Transport in c-BAs

We now move on to evaluate the accuracy of the GAP in predicting the phonon transport properties and thermal conductivity of pristine c-BAs. In Fig. 3(a) we compare the phonon dispersions predicted by the GAP and DFT. The phonon dispersion predicted by the GAP almost overlaps with the DFT result, indicating that the GAP can accurately reproduce the second-order IFCs of c-BAs. In Fig. 3(b) we present the κ of pristine c-BA predicted by the GAP and DFT as a function of temperature along with the experimental data [8–10]. As shown in Fig. 3(b), the κ considering only phonon-isotope and three-phonon scattering ($\kappa_{3\text{ph}}$) and that further considering four-phonon scattering ($\kappa_{3+4\text{ph}}$) predicted by the GAP agree reasonably with the DFT benchmarks. Meanwhile, the $\kappa_{3+4\text{ph}}$ predicted by the GAP falls within the range of the experimental values [8–10]. Particularly, the $\kappa_{3+4\text{ph}}$ predicted by the GAP and DFT both peaks at 20 K. We notice that the deviation between the $\kappa_{3\text{ph}}$ ($\kappa_{3+4\text{ph}}$) predicted by the GAP and DFT for temperatures around 20 K is relatively larger compared to that at higher temperatures. The maximum deviation of the $\kappa_{3\text{ph}}$ ($\kappa_{3+4\text{ph}}$) is 19.96% (19.97%) within 10–

90 K, while that is 4.08% (1.83%) for the temperatures above. The larger deviation for thermal conductivity around the peak value is expected considering that they are dominated by the contribution of low-frequency phonons, which can produce a larger error as temperature decreases. For example, a small deviation in the frequency can result in a larger change in the phonon population at lower temperatures.

Beyond the overall κ , the GAP also accurately predicts the spectral thermal conductivity of pristine c-BAs. Specifically, Fig. 4 shows the cumulative κ with respect to phonon MFP

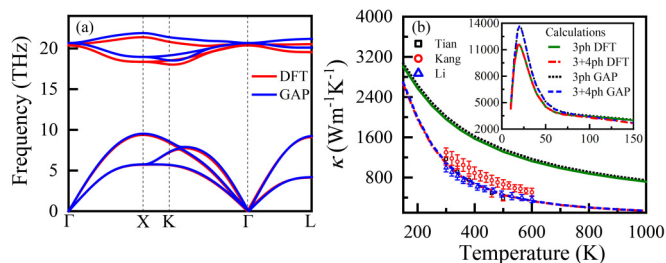


FIG. 3. (a) Phonon dispersion of c-BAs predicted by the GAP and DFT. (b) The κ of c-BAs with considering only three-phonon scattering (3ph) and both three-phonon and four-phonon scattering (3+4ph) as a function of temperature from the GAP and DFT, along with the experimental results reported by Kang *et al.* [8], Li *et al.* [9], and Tian *et al.* [10]. Insert: the $\kappa_{3\text{ph}}$ and $\kappa_{3+4\text{ph}}$ predicted by the GAP and DFT within the temperature range 10–150 K.

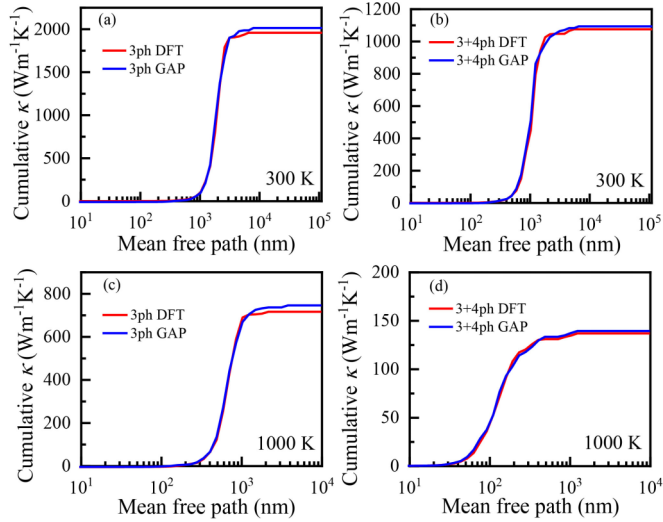


FIG. 4. Cumulative κ of c-BAs at 300 K predicted by the GAP and DFT as a function of phonon MFP with considering (a) only three-phonon scattering and (b) both three-phonon and four-phonon scattering. (c), (d) The same as (a), (b) but at 1000 K.

at 300 and 1000 K predicted by the GAP and DFT, which mostly overlap with each other. Moreover, the τ_{iso}^{-1} [Fig. 5(a)], $\tau_{3\text{ph}}^{-1}$, and $\tau_{4\text{ph}}^{-1}$ [the results at 300 K are shown as an example in Fig. 5(b)] predicted by the GAP show good agreement with the DFT benchmarks, demonstrating that the GAP can accurately reproduce phonon-isotope and high-order phonon-phonon interactions.

Compared with the pristine case, the *ab initio* PES of c-BAs with vacancies becomes more complicated as the structural disorder increases, placing a higher requirement for the precision of the GAP. As shown in Fig. 6, the $\tau_{\text{ph-v}}^{-1}$ for 0.01% ($3.65 \times 10^{18} \text{ cm}^{-3}$) As or B vacancy predicted by the GAP are in good agreement with the DFT benchmarks, indicating that the GAP can accurately predict the κ of c-BAs with vacancies. Also, the accurate prediction of the GAP for $\tau_{\text{ph-v}}^{-1}$ demonstrates its accuracy in predicting the harmonic IFCs of c-BAs with vacancies. In contrast to the τ_{iso}^{-1} that results from only mass difference, the $\tau_{\text{ph-v}}^{-1}$ is caused by only IFC perturbation, as indicated by Eqs. (9) and (10). We notice that the frequency dependence of both τ_{iso}^{-1} and $\tau_{\text{ph-v}}^{-1}$ is close to ω^4 at low frequency, indicating a typical behavior of Rayleigh

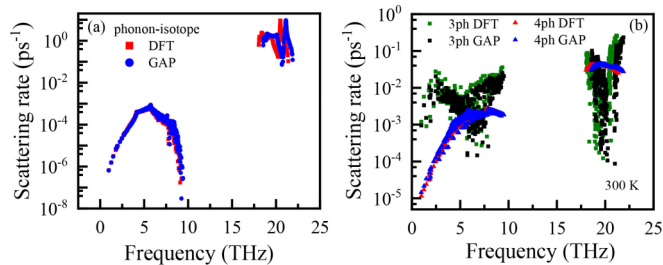


FIG. 5. (a) Phonon-isotope scattering rates of c-BAs predicted by the GAP and DFT. (b) Three-phonon scattering rates and four-phonon scattering rates of c-BAs predicted by the GAP and DFT at 300 K.

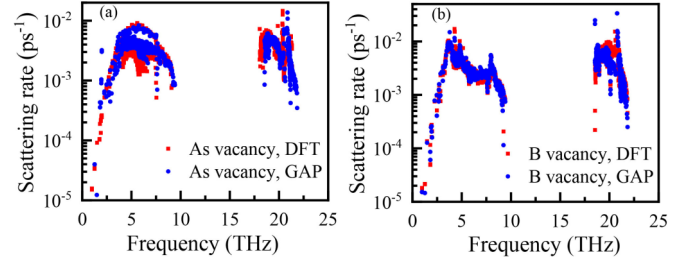


FIG. 6. Phonon-vacancy scattering rates for 0.01% ($3.65 \times 10^{18} \text{ cm}^{-3}$) As or (b) B vacancy concentration predicted by the GAP and DFT.

scattering in the long-wavelength limit (see Fig. S2 in the Supplemental Material [59]).

C. Computational Efficiency of the GAP

To evaluate the computational efficiency of the GAP, we performed AIMD simulations for a supercell of c-BAs containing 128 atoms in the *NVT* ensemble at 300 K with a time step of 0.5 fs. Employing one Intel Xeon Gold 5120 CPU (14 CPU cores), the computational time per time step was 171 (3152) s for AIMD simulations based on a $1 \times 1 \times 1$ ($2 \times 2 \times 2$) k mesh. In contrast, the classical MD simulations based on the GAP only take 0.228 s for one time step, which is 2–4 orders of magnitude faster than the AIMD simulations. Although the present GAP is considerably more efficient than DFT, it is still several orders of magnitude slower than empirical potentials, which typically provide six to eight orders of magnitude speed-up compared to *ab initio* calculations [63]. To expand the time and space scales of GAP, further improvements to its computational efficiency are necessary.

D. Competition between phonon-vacancy and four-phonon scattering

Using the developed GAP, we investigate the effect of vacancy on the κ and phonon scattering of c-BAs. Figure 7(a) shows the $\kappa_{3\text{ph}}$ and $\kappa_{3+4\text{ph}}$ of c-BAs predicted by the GAP as a function of vacancy concentration at 300 K. The values of $\kappa_{3\text{ph}}$ agree well with the previous DFT predictions [47]. Throughout the range of vacancy concentrations, the suppression of the $\kappa_{3\text{ph}}$ ($\kappa_{3+4\text{ph}}$) by B and As vacancies is almost the same. Note that the conventional models (such as the Ratsifaritana and Klemens model [64]) consider vacancies as effective mass perturbation and fail in predicting its effect on κ [22,47]. Specifically, the Ratsifaritana and Klemens model substantially underestimates (overestimates) the reduction of the κ by the B (As) vacancy, because the B vacancy is assumed to produce smaller mass perturbation than the As vacancy, as shown in the previous study [47]. As shown in Fig. 7(a), the $\kappa_{3+4\text{ph}}$ is much lower than the $\kappa_{3\text{ph}}$ for vacancy concentrations below 0.025% ($9.13 \times 10^{18} \text{ cm}^{-3}$), indicating a significantly stronger effect of four-phonon scattering than phonon-vacancy scattering. As the vacancy concentration increases above 0.07% ($2.56 \times 10^{19} \text{ cm}^{-3}$), the $\kappa_{3+4\text{ph}}$ gets close to the $\kappa_{3\text{ph}}$, indicating phonon-vacancy scattering becomes stronger than four-phonon scattering.

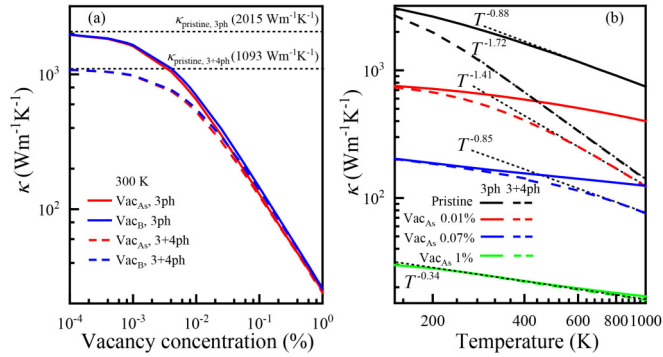


FIG. 7. (a) The κ of c-BAs with B or As vacancies predicted by the GAP as a function of vacancy concentration considering only three-phonon scattering and both three-phonon and four-phonon scattering at 300 K. The $\kappa_{3\text{ph}}$ and $\kappa_{3+4\text{ph}}$ of pristine c-BAs at 300 K is marked by black dotted lines. (b) The $\kappa_{3\text{ph}}$ and $\kappa_{3+4\text{ph}}$ of c-BAs with As vacancies as a function of temperature. The black solid (dashed) curve gives the $\kappa_{3\text{ph}}$ ($\kappa_{3+4\text{ph}}$) of vacancy-free c-BAs. The red, blue, and green solid (dashed) curves give the $\kappa_{3\text{ph}}$ ($\kappa_{3+4\text{ph}}$) of c-BAs with 0.01% (3.65 × 10¹⁸ cm⁻³), 0.07% (2.56 × 10¹⁹ cm⁻³), and 1% (3.65 × 10²⁰ cm⁻³) vacancies, respectively. The black dotted lines represent the temperature dependence of the κ of c-BAs.

To investigate the effect of vacancies on the temperature dependence of thermal conductivity in c-BAs, we calculated the $\kappa_{3\text{ph}}$ and $\kappa_{3+4\text{ph}}$ of c-BAs with vacancies as a function of temperature [Fig. 7(b)]. The comparison of the $\kappa_{3\text{ph}}$ and $\kappa_{3+4\text{ph}}$ in pristine c-BAs indicates that four-phonon scattering greatly increases the temperature dependence of thermal conductivity. Specifically, the temperature dependence of the $\kappa_{3+4\text{ph}}$ ($T^{-1.72}$) is substantially stronger than that of the $\kappa_{3\text{ph}}$ ($T^{-0.88}$) above 700 K (the calculated Debye temperature of c-BAs [65,66]) for the pristine material. In contrast to the four-phonon scattering, phonon-vacancy scattering can strongly decrease the temperature dependence of thermal conductivity, especially at low temperatures. This is expected, considering that three-phonon and four-phonon scattering become stronger with increasing temperature, whereas phonon-vacancy scattering is temperature independent. As the vacancy concentration increases to 0.01% (3.65 × 10¹⁸ cm⁻³), the temperature dependence of the $\kappa_{3+4\text{ph}}$ above 700 K becomes relatively weaker ($T^{-1.41}$) but still much stronger than that of the pristine $\kappa_{3\text{ph}}$ ($T^{-0.88}$), indicating stronger roles of four-phonon scattering in suppressing the thermal conductivity than phonon-vacancy scattering. When the vacancy concentration increases to 0.07%, the temperature dependence of the $\kappa_{3+4\text{ph}}$ above 700 K ($T^{-0.85}$) becomes close to that of the pristine $\kappa_{3\text{ph}}$ ($T^{-0.88}$), indicating a comparable effect of phonon-vacancy and four-phonon scattering. As the vacancy concentration further increases, the phonon-vacancy scattering becomes more dominant and results in a much weaker temperature dependence of thermal conductivity. For example, the $\kappa_{3+4\text{ph}}$ and $\kappa_{3\text{ph}}$ for 1% (3.65 × 10²⁰ cm⁻³) As vacancies mostly overlap with each other and exhibit a very weak temperature dependence ($\sim T^{-0.34}$) throughout the entire temperature range from 150 to 1000 K.

We continue to look into the spectral κ at 150 and 1000 K to understand the effect of vacancies on the temperature de-

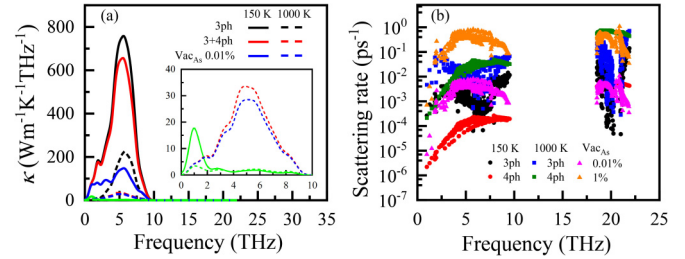


FIG. 8. (a) The spectral κ of c-BAs as a function of phonon frequency. The results at 150 K and 1000 K are given by the solid and dashed curves, respectively. Insert: zoom in for the spectral $\kappa_{3+4\text{ph}}$ of c-BAs within the frequency range 0–10 THz. (b) Modal phonon scattering rates as a function of frequency. Black (red) circles represent the $\tau_{3\text{ph}}^{-1}$ ($\tau_{4\text{ph}}^{-1}$) at 150 K, and the blue (green) squares represent the $\tau_{3\text{ph}}^{-1}$ ($\tau_{4\text{ph}}^{-1}$) at 1000 K. The $\tau_{\text{ph-v}}^{-1}$ for 0.01% (3.65 × 10¹⁸ cm⁻³) and 1% (3.65 × 10²⁰ cm⁻³) As vacancy concentrations is plotted by pink and orange triangles, respectively.

pendence of the κ in c-BAs. As shown in Fig. 8(a), the κ of c-BAs is mainly contributed by acoustic phonons < 9.8 THz. For the pristine case, four-phonon scattering results in $\sim 15\%$ reduction of the spectral $\kappa_{3+4\text{ph}}$ mainly within a small frequency range 4.5–7.5 THz at 150 K. In contrast, a much larger reduction ($\sim 82\%$) is observed for the spectral $\kappa_{3+4\text{ph}}$ at 1000 K, which occurs within a much broader frequency range from 2.0 to 9.8 THz. The sharp difference between the reduction at 150 and 1000 K can be explained by the temperature dependence of three-phonon and four-phonon scattering rates. As shown in Fig. 8(b), the $\tau_{4\text{ph}}^{-1}$ is about two orders of magnitude lower than the $\tau_{3\text{ph}}^{-1}$, except for the frequency range 4.5–7.5 THz at 150 K, accounting for the corresponding reduction of spectral $\kappa_{3+4\text{ph}}$. As the temperature increases to 1000 K, $\tau_{3\text{ph}}^{-1}$ and $\tau_{4\text{ph}}^{-1}$ increase by about two and one orders of magnitude, respectively. As a result, the $\tau_{4\text{ph}}^{-1}$ becomes comparable to or even larger than the $\tau_{3\text{ph}}^{-1}$ at 1000 K within 3.0–9.8 THz. This observation agrees with the scaling law of scattering rates derived in Ref. [27], i.e., $\tau_{4\text{ph}}^{-1} \propto T^2$ vs $\tau_{3\text{ph}}^{-1} \propto T$. When 0.01% vacancy is introduced, phonon-vacancy scattering leads to a remarkably larger reduction in the spectral $\kappa_{3+4\text{ph}}$ at 150 K ($\sim 74\%$ mainly within the frequency range 1.4–9.8 THz) than that at 1000 K ($\sim 13\%$ within 3.0–7.6 THz), which can be attributed to the relative strength of the $\tau_{\text{ph-v}}^{-1}$ as compared to the $\tau_{4\text{ph}}^{-1}$ and $\tau_{3\text{ph}}^{-1}$. Specifically, at 150 K the $\tau_{\text{ph-v}}^{-1}$ is comparable to or even larger than the dominant phonon-phonon scattering term $\tau_{3\text{ph}}^{-1}$, particularly within the frequency range 4.0–7.5 THz. In contrast, at 1000 K the $\tau_{\text{ph-v}}^{-1}$ is substantially lower than both the $\tau_{4\text{ph}}^{-1}$ and $\tau_{3\text{ph}}^{-1}$ within almost the entire frequency range, which explains the small influence of 0.01% vacancy on the temperature dependence of $\kappa_{3+4\text{ph}}$ above 700 K. As the vacancy concentration increases to 1%, phonon-vacancy scattering dominates over the phonon-phonon scattering within 2.0–9.8 THz at both 150 and 1000 K, resulting in $\sim 99\%$ and $\sim 91\%$ reduction of the spectral $\kappa_{3+4\text{ph}}$, respectively. Specifically, the $\tau_{\text{ph-v}}^{-1}$ is more than one order of magnitude larger than the $\tau_{4\text{ph}}^{-1}$ and $\tau_{3\text{ph}}^{-1}$ for most phonon modes within this frequency range even

at 1000 K. As a result, the corresponding spectral $\kappa_{3+4\text{ph}}$ at the two temperatures almost overlap with each other, as shown in the inset of Fig. 8(a). For the frequency range < 2.0 THz, the reduction of spectral $\kappa_{3+4\text{ph}}$ at 150 K ($\sim 89\%$) is substantially larger than that at 1000 K ($\sim 48\%$), because the $\tau_{\text{ph-v}}^{-1}$ for 1% vacancy is relatively larger than the $\tau_{3\text{ph}}^{-1}$ at 150 K but smaller than the $\tau_{3\text{ph}}^{-1}$ at 1000 K. Because of the dominance of phonon-vacancy scattering, 1% vacancy results in strongly suppressed thermal conductivity, exhibiting a close to temperature-independent behavior.

IV. CONCLUSIONS

In summary, we have developed a high-quality MLIP within the GAP framework for c-BAs with vacancies. The constructed GAP exhibits DFT-level accuracy in predicting the lattice thermal conductivity and phonon transport properties for c-BAs with vacancies, while its computational cost can be four orders of magnitude cheaper than DFT. Specifically, the GAP can accurately predict three-phonon, four-phonon, and phonon-vacancy scattering rates, demonstrating its accuracy in reproducing the harmonic IFCs of pristine and defective crystals, as well as the anharmonic IFCs up to fourth order of pristine crystals.

Using the developed GAP, we investigate the effect of vacancies on the thermal conductivity of c-BAs. Special attention was paid to the competition between phonon-vacancy and four-phonon scattering, which can decrease and increase the temperature dependence of κ , respectively. When the vacancy concentration is much lower than 0.07%, four-phonon scattering plays stronger roles in determining the temperature dependence of κ . For example, four-phonon scattering dom-

inates over the phonon-vacancy scattering at 0.01% vacancy concentration, resulting in a temperature dependence of the $\kappa_{3+4\text{ph}}$ ($T^{-1.41}$) close to that of the pristine $\kappa_{3+4\text{ph}}$ ($T^{-1.72}$) above 700 K. As the vacancy concentration increases to 0.07%, the temperature dependence of the $\kappa_{3+4\text{ph}}$ ($T^{-0.85}$) gets very close to that of the pristine $\kappa_{3\text{ph}}$ ($T^{-0.88}$) above 700 K, indicating comparable roles of phonon-vacancy and four-phonon scattering. As the vacancy concentration increases further, phonon-vacancy scattering becomes more dominant, resulting in a much weaker temperature dependence of κ . For instance, the $\kappa_{3+4\text{ph}}$ and $\kappa_{3\text{ph}}$ for 1% vacancy concentration exhibits an extremely weak temperature dependence ($\sim T^{-0.34}$) within the temperature range 150–1000 K, because the $\tau_{\text{ph-v}}^{-1}$ is more than one order of magnitude larger than the $\tau_{3\text{ph}}^{-1}$ and $\tau_{4\text{ph}}^{-1}$ for most phonon modes within 2.0–9.8 THz at temperatures up to 1000 K.

These results deepen the understanding of the phonon-scattering landscape in c-BAs with vacancies and will benefit the manipulation of its thermal properties. Atomistic simulations based on MLIPs can serve as a powerful tool to promote the understanding of thermal transport in defective materials.

ACKNOWLEDGMENTS

We acknowledge support from the Excellent Young Scientists Fund (Overseas) of Shandong Province (2022HWYQ-091), the Taishan Scholars Program of Shandong Province, the Natural Science Foundation of Shandong Province (ZR2022MA011), and the Initiative Research Fund of Shandong Institute of Advanced Technology. This work used the research computing facilities at Shandong Institute of Advanced Technology.

-
- [1] C. Freysoldt, B. Grabowski, T. Hickel, J. Neugebauer, G. Kresse, A. Janotti, and C. G. Van de Walle, First-principles calculations for point defects in solids, *Rev. Mod. Phys.* **86**, 253 (2014).
 - [2] E. G. Seebauer and M. C. Kratzer, Charged point defects in semiconductors, *Mater. Sci. Eng.: R: Rep.* **55**, 57 (2006).
 - [3] T. Zhu, L. Hu, X. Zhao, and J. He, New insights into intrinsic point defects in V_2VI_3 thermoelectric materials, *Adv. Sci.* **3**, 1600004 (2016).
 - [4] Y. Zhou, J. Chen, O. M. Bakr, and H. T. Sun, Metal-doped lead halide perovskites: Synthesis, properties, and optoelectronic applications, *Chem. Mater.* **30**, 6589 (2018).
 - [5] B. Tandon, S. L. Gibbs, B. Z. Zydlewski, and D. J. Milliron, Quantitative analysis of plasmonic metal oxide nanocrystal ensembles reveals the influence of dopant selection on intrinsic optoelectronic properties, *Chem. Mater.* **33**, 6955 (2021).
 - [6] Z. Bin, Z. Liu, Y. Qiu, and L. Duan, Efficient n dopants and their roles in organic electronics, *Adv. Opt. Mater.* **6**, 1800536 (2018).
 - [7] F. Zhang, H. L. Smith, and A. Kahn, Molecular dopants: Tools to control the electronic structure of metal halide perovskite interfaces, *Appl. Phys. Rev.* **8**, 041301 (2021).
 - [8] J. S. Kang, M. Li, H. Wu, H. Nguyen, and Y. Hu, Experimental observation of high thermal conductivity in boron arsenide, *Science* **361**, 575 (2018).
 - [9] S. Li, Q. Zheng, Y. Lv, X. Liu, X. Wang, P. Y. Huang, D. G. Cahill, and B. Lv, High thermal conductivity in cubic boron arsenide crystals, *Science* **361**, 579 (2018).
 - [10] F. Tian, B. Song, X. Chen, N. K. Ravichandran, Y. Lv, K. Chen, S. Sullivan, J. Kim, Y. Zhou, and T. H. Liu, Unusual high thermal conductivity in boron arsenide bulk crystals, *Science* **361**, 582 (2018).
 - [11] B. Lv, Y. Lan, X. Wang, Q. Zhang, Y. Hu, A. J. Jacobson, D. Broido, G. Chen, Z. Ren, and C. W. Chu, Experimental study of the proposed super-thermal-conductor: BAs, *Appl. Phys. Lett.* **106**, 074105 (2015).
 - [12] T. Xing, C. Zhu, Q. Song, H. Huang, J. Xiao, D. Ren, M. Shi, P. Qiu, X. Shi, and F. Xu, Ultralow lattice thermal conductivity and superhigh thermoelectric figure-of-merit in (Mg, Bi) Codoped GeTe, *Adv. Mater.* **33**, 2008773 (2021).
 - [13] X. Qian, J. Zhou, and G. Chen, Phonon-engineered extreme thermal conductivity materials, *Nat. Mater.* **20**, 1188 (2021).
 - [14] X. Gu and R. Yang, Phonon transport and thermal conductivity in two-dimensional materials, *Annu. Rev. Heat Transfer* **19**, 1 (2016).

- [15] R. O. Jones, Density functional theory: Its origins, rise to prominence, and future, *Rev. Mod. Phys.* **87**, 897 (2015).
- [16] D. A. Broido, M. Malorny, G. Birner, N. Mingo, and D. Stewart, Intrinsic lattice thermal conductivity of semiconductors from first principles, *Appl. Phys. Lett.* **91**, 231922 (2007).
- [17] J. Tersoff, Modeling solid-state chemistry: Interatomic potentials for multicomponent systems, *Phys. Rev. B* **39**, 5566 (1989).
- [18] V. Varshney, S. S. Patnaik, C. Muratore, A. K. Roy, A. A. Voevodin, and B. L. Farmer, MD simulations of molybdenum disulphide (MoS_2): Force-field parameterization and thermal transport behavior, *Comput. Mater. Sci.* **48**, 101 (2010).
- [19] S. Chen, Q. Wu, C. Mishra, J. Kang, H. Zhang, K. Cho, W. Cai, A. A. Balandin, and R. S. Ruoff, Thermal conductivity of isotopically modified graphene, *Nat. Mater.* **11**, 203 (2012).
- [20] S. G. Volz and G. Chen, Molecular dynamics simulation of thermal conductivity of silicon nanowires, *Appl. Phys. Lett.* **75**, 2056 (1999).
- [21] R. Stern, T. Wang, J. Carrete, N. Mingo, and G. K. H. Madsen, Influence of point defects on the thermal conductivity in FeSi, *Phys. Rev. B* **97**, 195201 (2018).
- [22] N. A. Katcho, J. Carrete, W. Li, and N. Mingo, Effect of nitrogen and vacancy defects on the thermal conductivity of diamond: An *ab initio* Green's function approach, *Phys. Rev. B* **90**, 094117 (2014).
- [23] C. A. Polanco and L. Lindsay, *Ab initio* phonon point defect scattering and thermal transport in graphene, *Phys. Rev. B* **97**, 014303 (2018).
- [24] N. Mingo, K. Esfarjani, D. A. Broido, and D. A. Stewart, Cluster scattering effects on phonon conduction in graphene, *Phys. Rev. B* **81**, 045408 (2010).
- [25] R. Guo and S. Lee, Mie scattering of phonons by point defects in IV-VI semiconductors PbTe and GeTe, *Mater. Today Phys.* **12**, 100177 (2020).
- [26] A. Kundu, N. Mingo, D. A. Broido, and D. A. Stewart, Role of light and heavy embedded nanoparticles on the thermal conductivity of SiGe alloys, *Phys. Rev. B* **84**, 125426 (2011).
- [27] T. Feng, L. Lindsay, and X. Ruan, Four-phonon scattering significantly reduces intrinsic thermal conductivity of solids, *Phys. Rev. B* **96**, 161201(R) (2017).
- [28] X. Yang, T. Feng, J. Li, and X. Ruan, Stronger role of four-phonon scattering than three-phonon scattering in thermal conductivity of III-V semiconductors at room temperature, *Phys. Rev. B* **100**, 245203 (2019).
- [29] N. K. Ravichandran and D. Broido, Phonon-Phonon Interactions in Strongly Bonded Solids: Selection Rules and Higher-Order Processes, *Phys. Rev. X* **10**, 021063 (2020).
- [30] S. G. Mayr, Y. Ashkenazy, K. Albe, and R. S. Averback, Mechanisms of Radiation-Induced Viscous Flow: Role of Point Defects, *Phys. Rev. Lett.* **90**, 055505 (2003).
- [31] M. I. Mendeleev, S. Han, W. j. Son, G. J. Ackland, and D. J. Srolovitz, Simulation of the interaction between Fe impurities and point defects in V, *Phys. Rev. B* **76**, 214105 (2007).
- [32] Y. Lee, S. Lee, and G. S. Hwang, Effects of vacancy defects on thermal conductivity in crystalline silicon: A nonequilibrium molecular dynamics study, *Phys. Rev. B* **83**, 125202 (2011).
- [33] B. Mortazavi and S. Ahzi, Thermal conductivity and tensile response of defective graphene: A molecular dynamics study, *Carbon* **63**, 460 (2013).
- [34] D. A. Terentyev, T. P. C. Klaver, P. Olsson, M. C. Marinica, F. Willaime, C. Domain, and L. Malerba, Self-Trapped Interstitial-Type Defects in Iron, *Phys. Rev. Lett.* **100**, 145503 (2008).
- [35] H. Babaei, R. Guo, A. Hashemi, and S. Lee, Machine-learning-based interatomic potential for phonon transport in perfect crystalline Si and crystalline Si with vacancies, *Phys. Rev. Mater.* **3**, 074603 (2019).
- [36] A. P. Bartók, M. C. Payne, R. Kondor, and G. Csányi, Gaussian Approximation Potentials: The Accuracy of Quantum Mechanics, Without the Electrons, *Phys. Rev. Lett.* **104**, 136403 (2010).
- [37] A. V. Shapeev, Moment tensor potentials: A class of systematically improvable interatomic potentials, *Multiscale Model. Simul.* **14**, 1153 (2016).
- [38] A. P. Thompson, L. P. Swiler, C. R. Trott, S. M. Foiles, and G. J. Tucker, Spectral neighbor analysis method for automated generation of quantum-accurate interatomic potentials, *J. Comput. Phys.* **285**, 316 (2015).
- [39] J. Behler and M. Parrinello, Generalized Neural-Network Representation of High-Dimensional Potential-Energy Surfaces, *Phys. Rev. Lett.* **98**, 146401 (2007).
- [40] Z. Fan, Z. Zeng, C. Zhang, Y. Wang, K. Song, H. Dong, Y. Chen, and T. Ala Nissila, Neuroevolution machine learning potentials: Combining high accuracy and low cost in atomistic simulations and application to heat transport, *Phys. Rev. B* **104**, 104309 (2021).
- [41] L. Zhang, J. Han, H. Wang, R. Car, and E. Weinan, Deep Potential Molecular Dynamics: A Scalable Model with the Accuracy of Quantum Mechanics, *Phys. Rev. Lett.* **120**, 143001 (2018).
- [42] J. Tang, G. Li, Q. Wang, J. Zheng, L. Cheng, and R. Guo, Effect of four-phonon scattering on anisotropic thermal transport in bulk hexagonal boron nitride by machine learning interatomic potential, *Int. J. Heat Mass Transf.* **207**, 124011 (2023).
- [43] B. Mortazavi, E. V. Podryabinkin, S. Roche, T. Rabczuk, X. Zhuang, and A. V. Shapeev, Machine-learning interatomic potentials enable first-principles multiscale modeling of lattice thermal conductivity in graphene/borophene heterostructures, *Mater. Horiz.* **7**, 2359 (2020).
- [44] Y. B. Liu, J. Y. Yang, G. M. Xin, L. H. Liu, G. Csányi, and B. Y. Cao, Machine learning interatomic potential developed for molecular simulations on thermal properties of $\beta\text{-Ga}_2\text{O}_3$, *J. Chem. Phys.* **153**, 144501 (2020).
- [45] X. Qian, S. Peng, X. Li, Y. Wei, and R. Yang, Thermal conductivity modeling using machine learning potentials: Application to crystalline and amorphous silicon, *Mater. Today Phys.* **10**, 100140 (2019).
- [46] J. George, G. Hautier, A. P. Bartók, G. Csányi, and V. L. Deringer, Combining phonon accuracy with high transferability in Gaussian approximation potential models, *J. Chem. Phys.* **153**, 044104 (2020).
- [47] N. H. Protik, J. Carrete, N. A. Katcho, N. Mingo, and D. Broido, *Ab initio* study of the effect of vacancies on the thermal conductivity of boron arsenide, *Phys. Rev. B* **94**, 045207 (2016).
- [48] P. Rowe, G. Csányi, D. Alfe, and A. Michaelides, Development of a machine learning potential for graphene, *Phys. Rev. B* **97**, 054303 (2018).
- [49] A. P. Bartók and G. Csányi, Gaussian approximation potentials: A brief tutorial introduction, *Int. J. Quantum Chem.* **115**, 1051 (2015).

- [50] A. P. Bartók, J. Kermode, N. Bernstein, and G. Csányi, Machine Learning a General-Purpose Interatomic Potential for Silicon, *Phys. Rev. X* **8**, 041048 (2018).
- [51] G. Kresse and J. Furthmüller, Efficiency of *ab-initio* total energy calculations for metals and semiconductors using a plane-wave basis set, *Comput. Mater. Sci.* **6**, 15 (1996).
- [52] G. Kresse and J. Furthmüller, Efficient iterative schemes for *ab initio* total-energy calculations using a plane-wave basis set, *Phys. Rev. B* **54**, 11169 (1996).
- [53] J. P. Perdew, K. Burke, and M. Ernzerhof, Generalized Gradient Approximation Made Simple, *Phys. Rev. Lett.* **77**, 3865 (1996).
- [54] S. i. Tamura, Isotope scattering of dispersive phonons in Ge, *Phys. Rev. B* **27**, 858 (1983).
- [55] A. Togo and I. Tanaka, First principles phonon calculations in materials science, *Scr. Mater.* **108**, 1 (2015).
- [56] S. Plimpton, Fast parallel algorithms for short-range molecular dynamics, *J. Comput. Phys.* **117**, 1 (1995).
- [57] W. Li, J. Carrete, N. A. Katcho, and N. Mingo, ShengBTE: A solver of the Boltzmann transport equation for phonons, *Comput. Phys. Commun.* **185**, 1747 (2014).
- [58] Z. Han, X. Yang, W. Li, T. Feng, and X. Ruan, Four-phonon: An extension module to ShengBTE for computing four-phonon scattering rates and thermal conductivity, *Comput. Phys. Commun.* **270**, 108179 (2022).
- [59] See Supplemental Material at <http://link.aps.org/supplemental/10.1103/PhysRevMaterials.7.044601> for the convergence of the lattice thermal conductivity of pristine c-BAs predicted by DFT with respect to the q mesh, and the phonon-isotope and phonon-vacancy scattering rates for 0.01%As and B vacancy concentration predicted by DFT.
- [60] Y. Zuo, C. Chen, X. Li, Z. Deng, Y. Chen, J. Behler, G. Csányi, A. V. Shapeev, A. P. Thompson, and M. A. Wood, Performance and cost assessment of machine learning interatomic potentials, *J. Phys. Chem. A* **124**, 731 (2020).
- [61] W. J. Szlachta, A. P. Bartók, and G. Csányi, Accuracy and transferability of Gaussian approximation potential models for tungsten, *Phys. Rev. B* **90**, 104108 (2014).
- [62] J. Byggmästar, K. Nordlund, and F. Djurabekova, Modeling refractory high-entropy alloys with efficient machine-learned interatomic potentials: Defects and segregation, *Phys. Rev. B* **104**, 104101 (2021).
- [63] C. W. Rosenbrock, K. Gubaev, A. V. Shapeev, L. B. Pártay, N. Bernstein, G. Csányi, and G. L. Hart, Machine-learned interatomic potentials for alloys and alloy phase diagrams, *npj Comput. Mater.* **7**, 24 (2021).
- [64] C. Ratsifaritana and P. Klemens, Scattering of phonons by vacancies, *Int. J. Thermophys.* **8**, 737 (1987).
- [65] S. Daoud, N. Bioud, and N. Bouarissa, Structural phase transition, elastic and thermal properties of boron arsenide: Pressure-induced effects, *Mater. Sci. Semicond. Proc.* **31**, 124 (2015).
- [66] L. Lindsay, D. Broido, and T. Reinecke, First-Principles Determination of Ultrahigh Thermal Conductivity of Boron Arsenide: A Competitor for Diamond? *Phys. Rev. Lett.* **111**, 025901 (2013).